Large topological Hall effect near room temperature in noncollinear ferromagnet LaMn₂Ge₂ single crystal

Gaoshang Gong,[1,2,*] Longmeng Xu,[1,*] Yuming Bai,[1] Yongqiang Wang,[2] Songliu Yuan,[1] Yong Liu,[3] and Zhaoming Tian ®[1,†]

[1]*School of Physics and Wuhan National High Magnetic Field Center, Huazhong University of Science and Technology, Wuhan 430074, People's Republic of China*
[2]*School of Physics and Electronic Engineering, Zhengzhou University of Light Industry, Zhengzhou 450002, People's Republic of China*
[3]*School of Physics, Wuhan University, Wuhan 430072, People's Republic of China*

Nontrivial spin structures in itinerant magnets can give rise to the topological Hall effect (THE) due to the interacting local magnetic moments and conductive electrons. While, in series of materials, THE has mostly been observed at low temperatures far below room temperature (RT) limiting its potential applications. Here, we report the anisotropic anomalous Hall effect (AHE) near RT in LaMn₂Ge₂, a noncollinear ferromagnetic compound with Curie temperature $T_C \sim 325$ K. A large topological Hall resistivity of $\sim 1.0\,\mu\Omega$ cm in a broad temperature range (190 K $< T <$ 300 K) is realized as field (H) is parallel to the ab plane ($H//ab$) and current along the c axis ($I//c$), in contrast to the conventional AHE for $H//c$ and $I//ab$. The emergence of THE is attributed to the spin chirality of noncoplanar spin configurations stabilized by thermal fluctuation during spin-flop process. Moreover, the constructed temperature-field (H-T) phase diagrams based on the isothermal topological Hall resistivity reveal a field-induced transition from the noncoplanar spin configuration to polarized ferromagnetic state. Our experimental realization of large THE near RT highlights LaMn₂Ge₂ as a promising system for functional applications in novel spintronic devices.

I. INTRODUCTION

The interplay between charge and spin degrees of freedom in itinerant magnets can generate various kinds of intriguing electromagnetic phenomena. As one typical example, the anomalous Hall effect (AHE) characterized by a transverse voltage generated by longitudinal charge current even at zero field in ferromagnetic (FM) metals [1–3], has attracted considerable attention from both the fundamental physics of magnetotransport and spintronic applications. As for its origin, two qualitatively different mechanisms are widely accepted, extrinsic impurity scattering processes and intrinsic contribution from band structure [3–5]. The extrinsic mechanisms involve the skew-scattering and side-jump scattering ones [6,7], which produce the AHE due to the asymmetric scattering of conduction electrons. The intrinsic Karplus-Luttinger mechanism is related to the spin-orbit interaction (SOI) and perturbation by the electric field initially proposed by Karplus and Luttinger [8], recent theories have reinterpreted it by invoking the Berry-phase concepts [9,10]. Compared to the AHE in conventional metallic ferromagnets, another unconventional Hall signal termed topological Hall effect (THE) can also arise in materials with nontrivial spin structures [11–14]. In such systems, the conduction electrons can acquire a nonzero Berry phase associated with finite scalar

spin chirality $\chi_{ijk} = S_i \cdot (S_j \times S_k)$ when passing through the localized spin moments (S_i, S_j, and S_k) [11,12], which acts as an emergent magnetic field responsible for the THE. In this mechanism, the magnitude of THE is related to the χ_{ijk} not M. Therefore, the total Hall resistivity (ρ_{xy}) in itinerant magnets should consist of three contributions expressed by $\rho_{xy} = R_0 \mu_0 H + R_S M + \rho_{xy}^T$, where the first, second, and third terms represent the normal, anomalous, and topological Hall resistivity, respectively. R_0 and R_S are the normal and anomalous Hall coefficients, respectively.

In experiment, THE has been widely reported in different systems hosting topologically nontrivial spin textures such as in magnetic skyrmions [13–15], double-exchanged ferromagnets [16,17], frustrated magnets [12,18–21], as well as artificial magnetic heterostructures [22,23]. Among them, frustrated magnets as ideal platform where the spins usually form noncollinear or noncoplanar configurations with nonzero χ_{ijk} are particularly attractive to explore THE, as reported in pyrochlore lattice Nd₂Mo₂O₇ and Pr₂Ir₂O₇ [11,12], triangular lattice PdCrO₂, and Gd₂PdSi₃ [24,25], Kagome lattice Mn₃Sn and Fe₃Sn₂ [26–28], etc. On the other side, the summation of χ_{ijk} over the whole lattice sites in frustrated magnets can also be macroscopically canceled out due to the lack of chiral magnetic symmetry, such as in ideal 120° spin structure [18,29], thereby THE is not a common feature among frustrated magnets. Moreover, limited by the low transition temperature, THE in most materials appears at temperatures far below room temperature (RT) hindering its practical applications, experimental realizations of large THE at RT in new materials

---

*These authors contributed equally to this work.
†Corresponding author: tianzhaoming@hust.edu.cn

034405-1
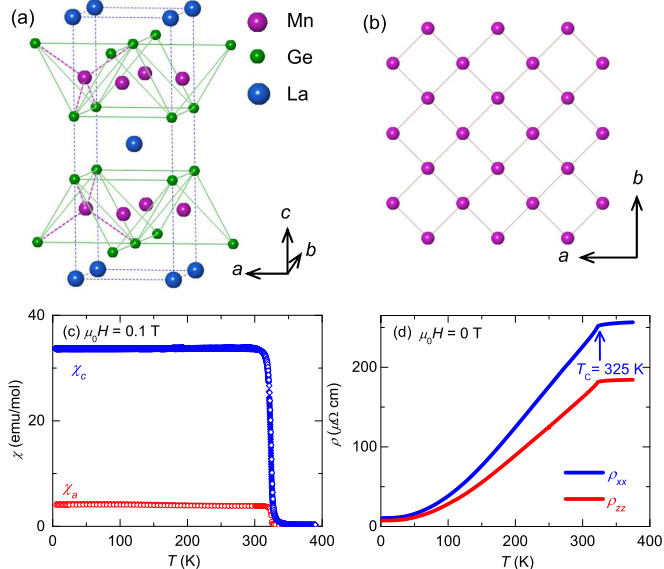
FIG. 1. (a) The crystal structure of $LaMn_2Ge_2$. Purple, green, and blue balls represent the Mn, Ge, and La atoms, respectively. (b) Top view of square layer of Mn atoms, (c) Temperature dependence of susceptibility $\chi(T)$ with ZFC and FC modes under $\mu_0H = 0.1$ T for $H//c$ and $H//a$ axis, respectively. (d) Temperature dependence of in-plane (ρ_{xx}) and out-of-plane (ρ_{zz}) longitudinal resistivity for the $I//a$ and c axis, respectively.

are highly appealing for its direct applications in spintronic devices.

$LaMn_2Ge_2$ belongs to a family of layered intermetallic compounds RM_2X_2 crystallized in $ThCr_2Si_2$-type structure with centrosymmetric tetragonal space group $I4/mmm$ (R: rare-earth element, M: $3d$ or $4d$ element and X: Si or Ge) [30], where magnetic Mn atoms are located on square-lattice sheets stacked parallelly along the c axis [see Figs. 1(a) and 1(b)]. Previous neutron scattering studies revealed the Mn moments formed the conical spin structure below Curie temperature $T_C \sim 325$ K [31], which couple ferromagnetically along easy c axis and antiferromagnetically within the ab plane. Considering the noncollinear magnetic ordering well above RT, $LaMn_2Ge_2$ provides a candidate to identify RT THE, motivating our present study.

Here, we investigate the anisotropic AHE up to RT in $LaMn_2Ge_2$ single crystals based on the systematical measurements of magnetic and electrical transport for field (H) along different directions. Compared to the observation of conventional AHE as H along c axis ($H//c$) and current (I) within the ab plane ($I//ab$), large topological hall resistivity of $\sim 1.0\,\mu\Omega$ cm extended up to RT is observed under $H//ab$ and $I//c$ axis. The emergence of THE is attributed to the scalar spin chirality due to the formation of noncoplanar spin configurations stabilized by thermal fluctuation during spin flop process.

II. EXPERIMENTAL DETAILS

Single crystals of $LaMn_2Ge_2$ were grown from the Indium flux. High-purity elements La(99.9%) and Mn(99.95%), Ge(99.99%), and In(99.99%) from Alfa Aesar in the molar ra-

tio La : Mn : Ge : In = 1 : 2 : 2 : 20 were put into an alumina crucible and sealed inside an evacuated ampoule. Then, it was heated at 1100 °C for 12 h, and cooled at a rate of 4 °C/h to 700 °C. At this temperature, the ampoule was taken out from the furnace rapidly and the Indium flux was decanted by a centrifuge, platelike crystals were obtained in a typical dimension of $0.5 \times 3 \times 3$ mm^3. The structure was characterized by x-ray diffraction collected with Cu K_α radiation at room temperature by using a diffractometer (Rigaku-TTR3), which confirmed the purity of samples.

Magnetic and electrical transport measurement were carried out using the superconducting quantum interference device magnetometer (Quantum Design) and commercial Physical Property Measurement System (Quantum Design), respectively. A standard four-probe method was used to perform the longitudinal and transverse electrical transport measurements with H always perpendicular to the I direction. Both the out-of-plane (ρ_{zz}, ρ_{zx}) and in-plane (ρ_{xx}, ρ_{xy}) electrical transports were measured with the $I//c$ axis and $I//ab$ plane, respectively. To eliminate the influence of contact electrode misalignments, Hall resistivity was measured for both field directions and symmetrized by $\rho_H(\mu_0H) = [\rho_H(+\mu_0H) - \rho_H(-\mu_0H)]/2$. All electrical transport measurements were repeated using crystals from the same batch with similar residual resistivity ratio (RRR), guaranteeing the reliability of experimental results.

III. RESULTS AND DISCUSSIONS

$LaMn_2Ge_2$ has a tetragonal structure with lattice constant $a = b = 4.19$ Å and $c = 10.95$ Å, where La, Mn, and Ge atoms occupy the Wyckoff positions $2a$ (0,0,0) $4d$ (0,0.5,0.25), and $4(e)$ (0,0,0.38), respectively. As depicted in Fig. 1(a), the La, Mn, and Ge atoms are located on separate layers alternating along the c axis in a sequence: -Mn-Ge-La-Ge-Mn-, where magnetic Mn layers are well separated by the nonmagnetic La and Ge layers [30]. In this structure, the $MnGe_4$ tetrahedra are connected in an edge-sharing fashion with the Mn atom at the center of each tetrahedron. Projection of $LaMn_2Ge_2$ on the (001) plane [shown in Fig. 1(b)], one can see the magnetic Mn atoms lay out on square lattice within the ab plane. The nearest Mn-Mn intralayer distance given by $a/\sqrt{2} = 2.97$ Å is much smaller than that of interlayer separation $c/2 = 5.48$ Å. For the crystals, the c axis is normal to the plane of plate.

Temperature (T) dependences of magnetic susceptibilities $\chi(T)$ for $LaMn_2Ge_2$ were measured under $H = 0.1$ T along a and c axis (χ_a and χ_c), respectively. For both directions, zero-field-cooled (ZFC) and field-cooled (FC) magnetization curves nearly overlap with slight differences at low temperatures. As shown in Fig. 1(c), a rapid upturn of χ_c is observed as T close to 325 K, characterizing the paramagnetic-ferromagnetic (PM-FM) transition at $T_c \sim 325$ K. Below T_c, χ_c is nearly ten times larger than χ_a, denoting the easy magnetization along c axis. The zero-field in-plane ρ_{xx} ($I//ab$) and out-of-plane resistivity ρ_{zz} ($I//c$) are also presented in Fig. 1(d), both curves exhibit metallic behaviors in all temperature regimes with large RRR $\rho(375\,\text{K})/\rho(10\,\text{K}) \sim 24$. A clear anomaly at ~ 325 K corresponds to the T_c, determined from $\chi(T)$ curves. The ratio of $\rho_{zz}(T)/\rho_{xx}(T) \sim 0.6-0.65$
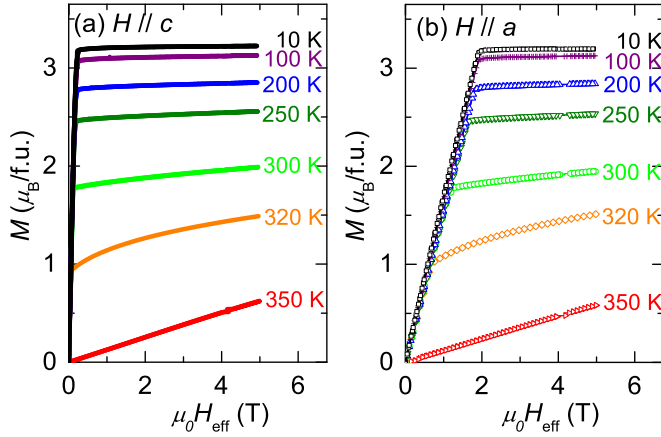
FIG. 2. The isothermal magnetization $M(\mu_0 H_{\mathrm{eff}})$ curves at different temperatures for (a) $H//c$ axis and (b) $H// a$ axis, respectively.

is almost temperature independent, reveals the in-plane and out-of-plane transport share the same scattering mechanism. The weak anisotropy implies three-dimensional (3D) electrical transport property rather than 2D ones.

Figures 2(a) and 2(b) exhibit the isothermal magnetization (M) curves at different temperatures for $H//c$ and $H//a$ axis, respectively. The magnetizations are plotted versus effective magnetic field ($\mu_0 H_{\mathrm{eff}}$) defined by $\mu_0 H_{\mathrm{eff}} = \mu_0(H - N_d M)$, where N_d is the demagnetization factor for samples in rectangular shape calculated by a method in Ref. [32]. For both directions with $T \ll T_C$, the magnetizations increase linearly at low fields and become saturated as the field above the saturation field ($\mu_0 H_s$). At $T = 10$ K, different saturation fields $\mu_0 H_s^c = 0.32$ T ($H//c$) and $\mu_0 H_s^a = 2.1$ T ($H//a$) reveal that LaMn$_2$Ge$_2$ has uniaxial magnetic anisotropy with easy axis along the c direction. The saturated magnetization $M_\mathrm{S} \sim 3.12\mu_\mathrm{B}$/f.u. is consistent with the previous reported value [33]. It is worthwhile to mention that we also measure the isothermal $M(\mu_0 H_{\mathrm{eff}})$ for H along different directions within the ab plane, which show almost isotropic behaviors.

LaMn$_2$Ge$_2$ displays strong anisotropic magnetotransport behaviors as H oriented along the c axis and within the ab plane. In Figs. 3(a) and 3(b), we firstly present the in-plane longitudinal magnetoresistance (MR) and Hall resistivity $\rho_{xy}(\mu_0 H_{\mathrm{eff}})$ data, respectively. During the measurements, the current is along a axis and field along c axis. Negative MRs $\{$MR $= [\rho(\mu_0 H) - \rho(0\mathrm{T})]/\rho(0\mathrm{T})\}$ are observed at high temperatures with maximum near T_c, (see Fig. 3(a) and Fig. S1 in Supplemental Material [34]), due to the suppression of spin-related scattering as usually observed in magnetic systems. As decreased temperature, MR changes sign to positive at low temperatures ($T < 60$ K), reflecting the dominant contribution of MR from the Lorenz force induced by H on the carrier motion. For field dependent Hall resistivity $\rho_{xy}(\mu_0 H_{\mathrm{eff}})$, it has a linear field dependence at $T > T_C$. Below T_c, $\rho_{xy}(\mu_0 H_{\mathrm{eff}})$ increases dramatically at low fields, then becomes slow at high fields with linear field dependence. As comparisons, the shape of $\rho_{xy}(\mu_0 H_{\mathrm{eff}})$ resembles the $M(\mu_0 H_{\mathrm{eff}})$ curve, suggesting the dominated conventional AHE as observed in FM metals. In this respect, Hall resistivity can be described by $\rho_{xy} = \rho_{xy}^N + \rho_{xy}^A = R_0\mu_0 H + R_S\mu_0 M$, where ρ_{xy}^N, ρ_{xy}^A, R_0, and
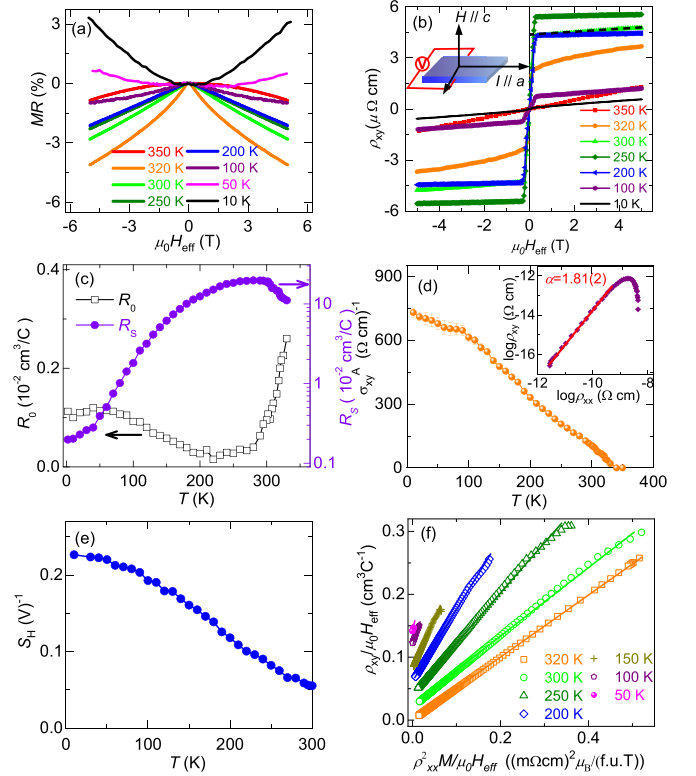
FIG. 3. Field dependence of (a) magnetoresistance and (b) Hall resistivity ρ_{xy} at selected temperatures under $H//c$ axis and $I//a$ axis, the inset shows the schematic setup of Hall resistivity measurements. (c) Temperature dependence of ordinary Hall coefficient R_0 and anomalous Hall coefficient R_S. (d) Temperature dependence of σ_{xy}^A, inset shows the plot of log ρ_{xy} versus log ρ_{xx}. (e) Temperature dependence of scaling coefficient S_H. (f) The scaling behavior of $\rho_{xy}/\mu_0 H_{\mathrm{eff}}$ versus $\rho_{xx}^2 M/\mu_0 H_{\mathrm{eff}}$ at indicated temperatures with subsequent offset of 0.02 cm^3 C^{-1} for clarity, solid lines represent linear fits of the data.

R_S represent the normal and anomalous Hall resistivity, and the normal and anomalous Hall coefficients, respectively. The value of R_0 and ρ_{xy}^A can be determined from the linear fit of $\rho_{xy}(\mu_0 H_{\mathrm{eff}})$ at the high-field regime [see Fig. 3(b)], namely, the slopes and y-axis intercepts correspond to the R_0 and ρ_{xy}^A, respectively. As shown in Fig. 3(c), a positive sign of R_0 in all temperatures reveals the dominant hole-type charge carrier. The carrier density n_a can be deduced by the single band model $n_a \sim -1/|e|R_0$, which reaches $5.6 \times 10^{21}\,\mathrm{cm}^{-3}$ at 10 K corresponding to ~1.1 carriers per formula unit of LaMn$_2$Ge$_2$. The extracted $R_\mathrm{S} \sim 0.2$ cm^3/C at 300 K from $\rho_{xy}^A = R_S\mu_0 M$ is about two order magnitude larger than that of usual FM materials, such as pure Fe and Ni ($T = 300$ K) [35,36]. Furthermore, both R_S and ρ_{xy}^A show broad humps at 280 K (see Fig. S2); this temperature is well below T_c, [$\sim0.85\,T_C$] similar to the observations in La$_{1-x}$Sr$_x$MnO$_3$ and Fe$_3$GeTe$_2$ single crystals [37,38].

To help to identify the dominant contribution of AHE, anomalous hall conductivity (AHC) σ_{xy}^A is evaluated by the relation $\sigma_{xy}^A = |\rho_{xy}/(\rho_{xx}^2 + \rho_{xy}^2)|$. As shown in Fig. 3(d) and Fig. S2, σ_{xy}^A at 10 K reaching up $\sim730\ \Omega^{-1}$ cm^{-1} is close to the expected value from the intrinsic Berry curvature
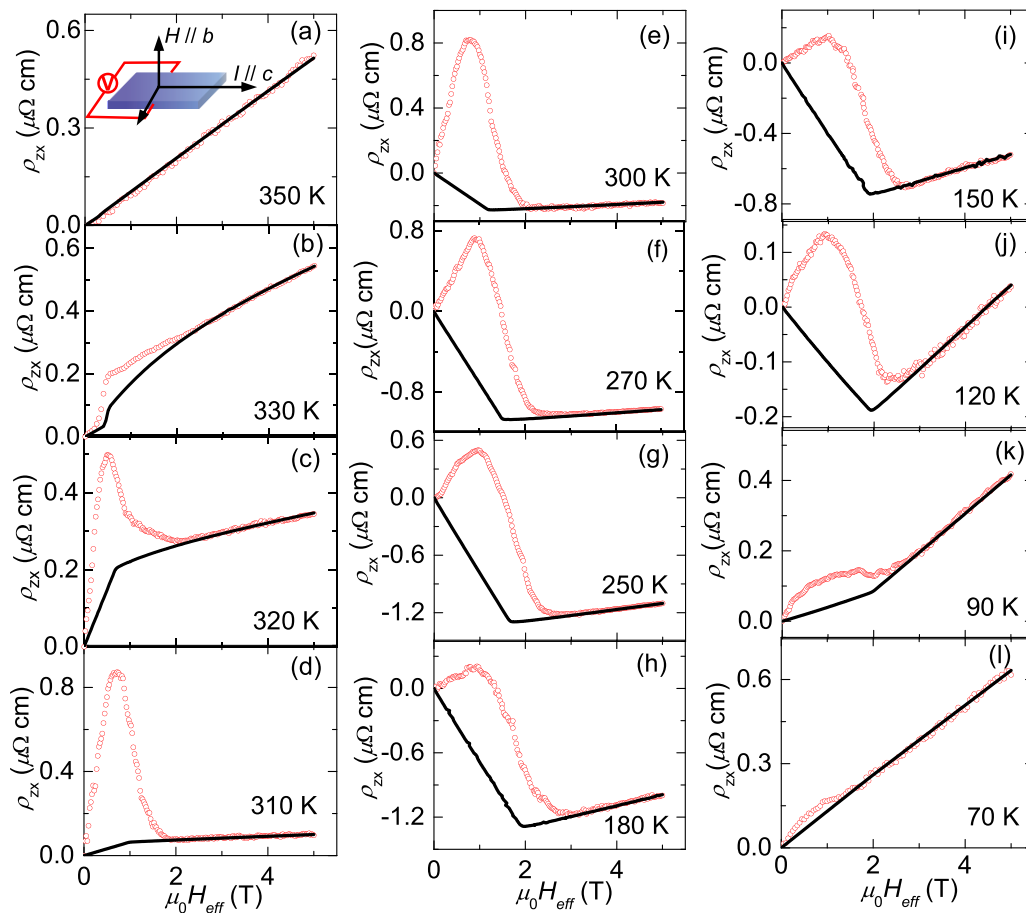
FIG. 4. (a)–(l) Isothermal Hall resistivity ρ_{zx} at various temperatures under the $H//a$ axis and $I//c$ axis, respectively. The black solid lines are the fitting curves including normal and anomalous Hall contributions.

contribution $\sigma_{xy,in}^A = e^2/(ha_z) \sim 704(2)$ Ω^{-1} cm^{-1} [5,39], where e is the electronic charge, h is the Plank constant, and $a_z = c/2 \sim 5.48(1)$ Å is the Mn interlayer's distance. This large σ_{xy}^A should not be from the extrinsic side-jump mechanism because it produces σ_{xy}^A in the order of $\frac{e^2}{ha_z}(\frac{E_{SO}}{E_F})$ (E_{SO} is the energy of SOC, E_F is the Fermi energy), where $\frac{E_{SO}}{E_F}$ usually has a value of $10^{-1} - 10^{-3}$ for metallic ferromagnets [3,7]. In terms of the extrinsic skew-scattering mechanism, σ_{xy}^A only can induce $e^2/(ha_z)$ in the ultraclean limit with $E_{SO} \gg \hbar/\tau$ (E_{SO} is the energy of SOC, τ is the scattering time), whose typical conductivity (G_{xx}) is $\sim 10^{-1}$ (S/sheet). [40] However, LaMn$_2$Ge$_2$ has the conductivity of $G_{xx} \sim 5 \times 10^{-3}$ (S/sheet) at 10 K in the moderately dirty regime ($E_{SO} \sim \hbar/\tau$). Additionally, the scaling coefficient $S_H = \mu_0 R_S/\rho_{xx}^2 = \sigma_{xy}^A/M$ corresponds to the sensitivity of AHC with respect to M. As shown in Fig. 3(e), the derived large value of $S_H \sim 0.22(2)$ V^{-1} at 10 K also supports that LaMn$_2$Ge$_2$ is in the moderately dirty region with relatively high conductivity in ferromagnets such as Fe$_3$Sn$_2$ ($S_H \sim 0.1$) and PrAlGe ($S_H \sim 0.15$ V^{-1}) [41,42]. In this regime, the skew-scattering contribution is much smaller than the intrinsic mechanism. Moreover, to discriminate the mechanism of AHE, a scaling relation analysis between ρ_{xy}^A and ρ_{xx}^α was usually used. [3,40] For LaMn$_2$Ge$_2$, the variation of log ρ_{xy}^A versus log ρ_{xx}

fitted by formula $\rho_{xy}^A \propto \rho_{xx}^\alpha$ gives the scaling exponent $\alpha = 1.81(\sim 2)$ [see the inset of Fig. 3(e)], ruling out the skew-scattering mechanism with a relation $\rho_{xy}^A \propto \rho_{xx}$ [6]. To further check whether ρ_{xy}^A has a quadratic dependence on ρ_{xx}, we plot $\rho_{xy}^A/\mu_0 H_{eff}$ vs $\rho_{xx}^2 M/\mu_0 H_{eff}$ at several temperatures [in Fig. 3(f)]. For clarification, the curves have been offset subsequently by 0.02 cm^3 C^{-1}. The good linear scaling of the data further corroborates dominant intrinsic mechanism of AHE. Thus, we argue that the main source of AHE is from the intrinsic Berry curvature contribution based on the scaling relation analysis, and future electronic band structure calculations will help to shed light on its mechanism.

Now, we turn to Hall effect for field oriented within the ab plane. Figures 4(a)–4(l) show the isothermal Hall resistivity $\rho_{zx}(\mu_0 H_{eff})$ data measured under $I//c$ and $H//b$, where the black lines represent the fitting curves by relation $\rho_{zx} = R_0 \mu_0 H + S_H \rho_{zz}^2 M$ with fitting parameter R_0 and S_H. At $T = 350$ K ($T > T_C$), linear field dependence of $\rho_{zx}(\mu_0 H_{eff})$ indicates the dominant normal Hall effect (NHE). As T approaches T_c, $\rho_{zx}(\mu_0 H_{eff})$ start to deviate from the scaling of $M(\mu_0 H_{eff})$ curves. Below T_c, this deviation becomes more obvious. More importantly, $\rho_{zx}(\mu_0 H_{eff})$ exhibit nontrivial field dependence with an abnormal broad peak at low-field regions ($H < H_s^a$) at which no anomaly is observed in the $M(\mu_0 H_{eff})$ curves. This unconventional behavior strongly supports the
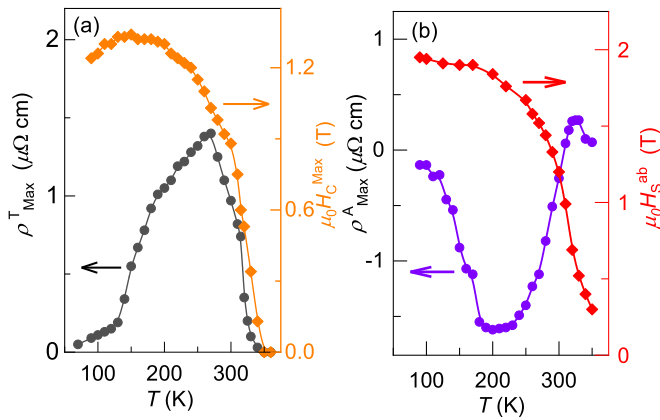
FIG. 5. (a) Temperature dependence of maximum amplitude of THE (ρ_{Max}^T) and corresponding field position ($\mu_0 H_C^{Max}$), (b) Temperature dependence of maximum values of AHE (ρ_{Max}^A) and saturated field ($\mu_0 H_s^{ab}$).

FIG. 6. (a) Contour plots of topological Hall resistivity versus temperature and field for LaMn$_2$Ge$_2$ under $H//a$ axis. The transition between noncoplanar spin structure and polarized FM order is marked by orange circles ($\mu_0 H_s^{ab}$), (b) The Mn moment projects for adjacent layers within ab plane (left side), ϕ is the angle between two magnetic moments at "1" and "1'" sites in the ab plane. The schematic spin configurations of Mn moments at $\mu_0 H = 0$ T, $0 < \mu_0 H < \mu_0 H_s^{ab}$ and $\mu_0 H > \mu_0 H_s^{ab}$ for $H//a$ axis (right side).

existence of an additional THE response besides the NHE and AHE contributions, different from the Hall response well described by the NHE and AHE contributions for $H//c$. By including THE, the total Hall resistivity ρ_{zx} of LaMn$_2$Ge$_2$ can be depicted by $\rho_{zx} = \rho_{zx}^N + \rho_{zx}^A + \rho_{zx}^T = R_0\mu_0 H + S_H\rho_{zz}^2 M + \rho_{zx}^T$, where ρ_{zx}^N, ρ_{zx}^A and ρ_{zx}^T represent the normal, anomalous, and topological Hall resistivity, respectively. Since ρ_{zx}^T should vanish when the full-polarized FM state is established as the field above critical field ($\mu_0 H_S^T$), we can determine the coefficients R_0 and S_H as the slope and intercept of the curve ρ_{zx} $vs \rho_{zz}^2 M$ above the critical field $\mu_0 H_S^a$. Using this analysis, ρ_{zx}^A(second term in above equation, $\rho_{zx}^A = S_H\rho_{zz}^2 M$) can be obtained. Afterwards, the ρ_{zx}^T component is separated by subtracting the normal and anomalous parts from measured $\rho_{zx}(\mu_0 H_{eff})$ curves (see Fig. S3). The maximum amplitude of THE (ρ_{Max}^T) and AHE (ρ_{Max}^A) as function of temperature are summarized in Figs. 5(a) and 5(b). As seen, ρ_{zx}^A reaches a maximum at the field ($\mu_0 H_T^{Max}$) smaller than $\mu_0 H_s^a$, which reveals a THE to emerge during the spin-flop process. Remarkably, large topological Hall resistivity $\rho_{Max}^T \sim 1.0\ \mu\Omega$ cm over broad temperature regions (190 K $< T <$ 300 K) is obtained, this value is in the same order of magnitude as recent report in bulk Heusler compound Mn$_2$PtSn (1.5 $\mu\Omega \cdot$cm) [43] and triangular-lattice Gd$_3$PdSi$_3$ magnet (2.6 $\mu\Omega$ cm) [25] but is nearly 20 times larger than that in noncollinear antiferromagnetic Mn$_5$Si$_3$ films ($\sim$0.05 $\mu\Omega$ cm) [19]. Moreover, the window temperature of THE in LaMn$_2$Ge$_2$ is enhanced up to RT, making it more attractive for potential spintronic applications. To more clearly present the variation of THE, the contour plot of the field-temperature (H-T) phase diagram using extracted THE data are constructed, shown in Fig. 6(a). Nonzero ρ_{zx}^T is detected at low-field regions ($\mu_0 H < \mu_0 H_S^T$) and high temperatures. As decreased temperature decreased, ρ_{zx}^T becomes zero at low temperatures ($T < \sim$70 K).

As for the origin of THE, it is generally attributed to the spin chirality by noncoplanar spin textures [13–21]. For LaMn$_2$Ge$_2$, previous neutron diffraction studies reveal it forms noncollinear conical magnetic structures at zero field for $T < T_C$ [31], where the FM component is along the lon-

gitudinal c axis (spin propagation direction) and the helical AFM component lies within the basal ab plane presented in Fig. 6(b) [31]. As H is applied along the ab plane, the conical spin configurations on the Mn sublattice will flop from c axis to ab plane, then the axis of the spiral structure has a tilting toward the ab plane and magnetic moments gain the net component in the ab plane leading to the formation of noncoplanar spin configurations. It further evolves into possible transverse conical magnetic structure [See Fig. 6(b)]. During the spin flop, due to the presence of tilted angles between adjacent Mn layers in the projected ab plane [see the left side of Fig. 6(b)], nonzero chiral spin configurations will be formed, producing an emergent magnetic field (B_{eff}) for conductive electrons responsible for THE. The amplitude of B_{eff} depends on the configuration of spins on the square lattice. Considering that topological Hall resistivity generated by B_{eff} can be expressed by $\rho_{zx}^T = PR_0 B_{eff}$ [13,44], where P is the spin polarization of charge carriers and R_0 denotes the normal Hall coefficient. At 300 K, the maximum value of B_{eff} can be estimated $\sim$95 T if we take $P \sim 0.65$ at H_T^{Max} and $R_0 = 0.016\ \mu\Omega$ cm/T (see Fig. S1). At H_T^{Max}, THE reaches maximum. Further increasing the field above $\mu_0 H_s^T$, a full polarized FM state is established leading to the vanishing of B_{eff} and THE. Thus, $\mu_0 H_S^T$ determines the phase boundary of magnetic transition from the noncoplanar spin configuration to the polarized FM state in the H-T phase diagram. Additionally, for the origin of THE, we would like to highlight the
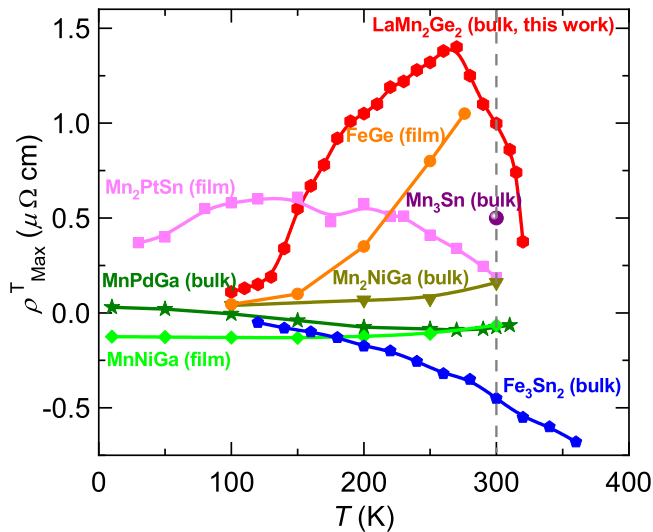
FIG. 7. Comparisons of ρ^T_{Max} for various materials exhibiting RT THE related to the noncoplanar spin textures. The data are taken from the open literatures, including Refs. [28,47–52]. The vertical dashed line represents the position of 300 K.

thermal-driven chiral spin fluctuation mechanism but not the static noncoplanar spin configuration as reported in triangular-lattice Gd_3PdSi_3 [25] and Fe_3GeTe_2 [38] magnets, since a THE in $LaMn_2Ge_2$ is only observed at high temperatures instead of low temperatures. Similar nontrivial skyrmion-lattice textures stabilized by thermal fluctuation in MnSi [45] and chiral spin fluctuations in $SrRuO_3$ films [46] have been proposed for a THE. Here, we propose that transverse conical spin fluctuation may be responsible for a THE in $LaMn_2Ge_2$ at elevated temperatures.

In comparison with the low temperature THE observed in majority of frustrated magnets, the realization of RT THE is critical to design novel spintronic devices based on THE. Here, the observed RT THE in $LaMn_2Ge_2$ is quite large

when compared to the limited materials hosting THE near RT, such as bulk Mn_3Sn [47], MnPdGa [48], Mn_2NiGa [49], and Fe_3Sn_2 [28], films of Mn_2PtSn [50], FeGe [51], and MnNiGa [52] (shown in Fig. 7). In $LaMn_2Ge_2$, THE component dominates the Hall effect at low fields while AHE reaches a maximum at high-field region. More importantly, THE has a much larger value than AHE, as example, the calculated maximum topological Hall conductivity (THC) $\sigma^T_{Max} \sim 45\ \Omega^{-1}\ cm^{-1}$ is four times the value of AHC $\sigma^A_{Max} \sim 12\Omega^{-1}cm^{-1}$ at 300 K (see Fig. S3). This is also different from the Hall effect observed in most Heusler compounds hosting Skyrmion lattice where the AHE is usually larger than THE [48–51]. Thus, it is a promising material for technological applications in spintronic devices based on THE.

IV. CONCLUSIONS

In summary, we reported a strong anisotropic Hall effect in a noncollinear ferromagnetic $LaMn_2Ge_2$ with $T_C \sim 325$ K. As $H//c$ and $I//ab$, it exhibits the conventional AHE dominated by the intrinsic Berry curvature mechanism. While, for $H//ab$ and $I//c$, large topological Hall resistivity in a broad field and temperature (190 K $< T < 310$ K) window can be observed, which arise from the formation of noncoplanar spin configuration with finite chirality stabilized by thermal fluctuations. The realization of large THE near RT in $LaMn_2Ge_2$ shows it to be a candidate material for practical applications in the THE-based spintronic devices.

[1] E. H. Hall, Am. J. Math. **2**, 287 (1879).

[2] E.H. Hall, Philos. Mag. **12**, 157 (1881).

[3] N. Nagaosa, J. Sinova, S. Onoda, A. H. MacDonald, and N. P. Ong, Rev. Mod. Phys. **82**, 1539 (2010).

[4] S. Onoda, N. Sugimoto, and N. Nagaosa, Phys. Rev. Lett. **97**, 126602 (2006).

[5] D. Xiao, M.C. Chang, and Q. Niu, Rev. Mod. Phys. **82**, 1959 (2010).

[6] J. Smit, Physica **24**, 39 (1958).

[7] L. Berger, Phys. Rev. B **2**, 4559 (1970).

[8] R. Karplus and J. M. Luttinger, Phys. Rev. **95**, 1154 (1954).

[9] G. Sundaram and Q. Niu, Phys. Rev. B **59**, 14915 (1999).

[10] T. Jungwirth, Q. Niu, and A. H. MacDonald, Phys. Rev. Lett. **88**, 207208 (2002).

[11] Y. Taguchi, Y. Oohara, H. Yoshizawa, N. Nagaosa, and Y. Tokura, Science **291**, 2573 (2001).

[12] Y. Machida, S. Nakatsuji, Y. Maeno, T. Tayama, T. Sakakibara, and S. Onoda, Phys. Rev. Lett. **98**, 057203 (2007).

[13] A. Neubauer, C. Pfleiderer, B. Binz, A. Rosch, R. Ritz, P. G. Niklowitz, and P. Böni, Phys. Rev. Lett. **102**, 186602 (2009).

[14] T. Schulz, R. Ritz, A. Bauer, M. Halder, M. Wagner, C. Franz, C. Pfleiderer, K. Everschor, M. Garst, and A. Rosch, Nat. Phys. **8**, 301 (2012).

[15] N. Kanazawa, Y. Onose, T. Arima, D. Okuyama, K. Ohoyama, S. Wakimoto, K. Kakurai, S. Ishiwata, and Y. Tokura, Phys. Rev. Lett. **106**, 156603 (2011).

[16] L. M. Wang, Phys. Rev. Lett. **96**, 077203 (2006).

[17] L. Vistoli, W. Wang, A. Sander, Q. Zhu, B. Casals, R. Cichelero, A. Barthélémy, S. Fusil, G. Herranz, S. Valencia, R. Abrudan, E. Weschke, K. Nakazawa, H. Kohno, J. Santamaria, W. Wu, V. Garcia, and M. Bibes, Nat. Phys. **15**, 67 (2019).

[18] Y. Shiomi, M. Mochizuki, Y. Kaneko, and Y. Tokura, Phys. Rev. Lett. **108**, 056601(2012).

[19] C. Sürgers, G. Fischer, P. Winkel, and H. V. Löhneysen, Nat. Commun. **5**, 3400 (2014).

[20] T. Suzuki, R. Chisnell, A. Devarakonda, Y.T. Liu, W. Feng, D. Xiao, J.W. Lynn, and J.G. Checkelsky, Nat. Phys. **12**, 1119 (2016).

[21] H. Li, B. Ding, J. Chen, Z. Li, E. Liu, X. Xi, G. Wu, and W. Wang, Appl. Phys. Lett. **116**, 182405 (2020).

[22] Q. Shao, Y. Liu, G. Yu, S. Kim, X. Che, C. Tang, Q. He, Y. Tserkovnyak, J. Shi, and K. Wang, Nat. Electron. **2**, 182 (2019).

[23] J. Matsuno, N. Ogawa, K. Yasuda, F. Kagawa, W. Koshibae, N. Nagaosa, Y. Tokura, and M. Kawasaki, Sci. Adv. **2**, e1600304 (2016).

[24] H. Takatsu, S. Yonezawa, S. Fujimoto, and Y. Maeno, Phys. Rev. Lett. **105**, 137201 (2010).

[25] T. Kurumaji, T. Nakajima, M. Hirschberger, A. Kikkawa, Y. Yamasaki, H. Sagayama, H. Nakao, Y. Taguchi, T. Arima, and Y. Tokura, Science **365**, 914 (2019).

[26] X. Li, L. Xu, L. Ding, J. Wang, M. Shen, X. Lu, Z. Zhu, and K. Behnia, Phys. Rev. Lett. **119**, 056601 (2017).

[27] P. K. Rout, P. V. Prakash Madduri, S. K. Manna, and A. K. Nayakx, Phys. Rev. B **99**, 094430 (2019).

[28] H. Li, B. Ding, J. Chen, Z. Li, Z. Hou, E. Liu, H. Zhang, X. Xi, G. Wu, and W. Wang, Appl. Phys. Lett. **114**, 192408 (2019).

[29] O. Masaru and N. Naoto, J. Phys. Soc. Jpn. **73**, 2624 (2004).

[30] Z. Ban and M. Sikirica, Acta Crystallogr. **18**, 594 (1965).

[31] G. Venturini, R. Welter, E. Ressouche, and B. Malaman, J. Alloy Compd, **210**, 213 (1994).

[32] A. Aharoni, J. Appl. Phys. **83**, 3432 (1998).

[33] T. Shigeoka, N. Iwata, H. Fujii, and T. Okamoto, J. Magn. Magn. Mater. **53**, 83 (1985).

[34] See Supplemental Material at http://link.aps.org/supplemental/10.1103/PhysRevMaterials.5.034405 for the temperature dependence of magnetoresistance, normal Hall coefficient and anomalous Hall resistiviy with field along different directions, and the isothermal anomalous Hall resistivity and topological Hall resistivity at different temperatures.

[35] N. V. Volkenshtein and G. V. Fedorov, Sov. Phys.-JETP **11**, 48 (1960).

[36] S. N. Kaul. Phys. Rev. B **20**, 5122 (1979).

[37] Y. Onose and Y. Tokura, Phys. Rev. B **73**, 174421 (2006).

[38] Y. Wang, C. Xian, J. Wang, B. Liu, L. Ling, L. Zhang, L. Cao, Z. Qu, and Y. Xiong, Phys. Rev B **96**, 134428 (2017).

[39] K. Manna, Y. Sun, L. Muechler, J. Kübler, and C. Felser, Nat. Rev. Mater. **3**, 244 (2018).

[40] S. Onoda, N. Sugimoto, and N. Nagaosa, Phys. Rev. B **77**, 165103 (2008).

[41] Q. Wang, S. Sun, X. Zhang, F. Pang, and H. Lei, Phys. Rev. B **94**, 075135(2016).

[42] B. Meng, H. Wu, Y. Qiu, C. Wang, Y. Liu, Z. Xia, S. Yuan, H. Chang, and Z. Tian, APL Mater. **7**, 051110 (2019).

[43] Z. Liu, A. Burigu, Y. Zhang, H. Jafri, X. Ma, E. Liu, W. Wang, and G. Wu, Scrip. Mater. **143**, 122 (2018).

[44] R. Ritz, M. Halder, C. Franz, A. Bauer, M. Wagner, R. Bamler, A. Rosch, and C. Pfleiderer, Phys. Rev. B **87**, 134424 (2013).

[45] S. Mühlbauer, B. Binz, F. Jonietz, C. Pfleiderer, A. Rosch, A. Neubauer, R. Georgii, and P. Böni, Science **323**, 915 (2009).

[46] W. Wang, M.W. Daniels, Z. Liao, Y. Zhao, J. Wang, G. Koster, G. Rijnders, C. Chang, D. Xiao, and W. Wu, Nat. Mater. **18**, 1054 (2019).

[47] X. Li, C. Collignon, L. Xu, H. Zuo, A. Cavanna, U. Gennser, D. Mailly, B. Fauqué, L. Balents, Z. Zhu, and K. Behnia, Nat. Comm. **10**, 3021 (2019).

[48] X. Xiao, L. Peng, X. Zhao, Y. Zhang, Y. Dai, J. Guo, M. Tong, J. Li, B. Li, W. Liu, J. Cai, B. Shen, and Z. Zhang, Appl. Phys. Lett. **114**, 142404 (2019).

[49] S. Sen, C. Singh, P. K. Mukharjee, R. Nath, and A. K. Nayak, Phys. Rev. B **99**, 134404 (2019).

[50] Y. Li, B. Ding, X. Wang, H. Zhang, W. Wang, and Z. Liu, Appl. Phys. Lett. **113**, 062406 (2018).

[51] J.C. Gallagher, K. Y. Meng, J. T. Brangham, H.L. Wang, B. D. Esser, D. W. McComb, and F. Y. Yang, Phys. Rev. Lett. **118**, 027201(2017).

[52] B. Ding, Y. Li, G. Xu, Y. Wang, Z. Hou, E. Liu, Z. Liu, G. Wu, and W. Wang, Appl. Phys. Lett. **110**, 092404 (2017).